OPEN ACCESS
IOP Publishing
Superconductor Science and Technology
Supercond. Sci. Technol. **36** (2023) 075009 (14pp)
https://doi.org/10.1088/1361-6668/acd27c

Performance review of the joints for the ITER poloidal field coils

M Breschi[1], L Cavallucci[1,*], H Adeagbo[1], K Sedlak[2], H Bajas[2], A Vostner[3] and Y Ilyin[3]

[1] DEI, Department of Electrical, Electronic and Information Engineering, University of Bologna, Bologna, Italy
[2] Ecole Polytechnique Federale de Lausanne (EPFL), Swiss Plasma Center (SPC), Villigen, CH 5232, Switzerland
[3] ITER Organization, Route de Vinon-sur-Verdon, CS 90 046, 13067 St. Paul Lez Durance Cedex, France

E-mail: lorenzo.cavallucci3@unibo.it

Received 2 March 2023, revised 24 April 2023
Accepted for publication 4 May 2023
Published 1 June 2023

Abstract

For large scale magnets wound with cable-in-conduit conductors, the safe operation of the joints is of paramount importance to guarantee adequate reliability and stability margin of the whole magnet. For this reason, during the R&D activities undertaken for the development of the ITER magnet system, several experimental campaigns were launched to study the AC and DC performance of the joint and limit the risk of thermal runaways at the joints during the tokamak operation. The joint electrical resistance must be limited below specified values to avoid excessive heating generated by the transport current. Moreover, in presence of time-varying fields, different types of losses arise at the joints, which can be associated to their superconducting and resistive parts. The relative importance of these losses depends on the joint manufacturing solution. The aim of this investigation is to analyze the performance at different working conditions of the joints for the connection of the conductors of the poloidal field (PF) coils of the ITER magnet system. This work presents, for the first time, a wide review of the test campaign performed from 2016 to 2021 on the PF joint samples during the three manufacturing phases, namely pre-qualification, qualification and production. The values of electrical resistances and losses under sinusoidal field variations are reported in the paper at different operating conditions, thus building a useful database to assess the joint performances during the machine operation. The data here collected show the impact of the manufacturing techniques on the joint performances and, furthermore, represent a useful tool for the validation of numerical and analytical models of joints.

Keywords: ITER project, joint, poloidal field coils, NbTi

(Some figures may appear in colour only in the online journal)

* Author to whom any correspondence should be addressed.

1. Introduction

The poloidal field (PF) coils of the ITER magnet system [1] are composed of six pancake coils operating with pulsed magnetic field to stabilize and shape the plasma [2–8]. The pancakes of the PF coils, wound with NbTi cable in conduit conductors (CICCs), will be connected in series by means of joints between the conductors [9].

The design of the PF joints is based on the twin-box layout [10–18] either in the 'shaking hands' or in the 'praying hands' configuration [19]. The two NbTi cables are connected by a saddle composed of two copper soles soldered together with a copper shim in between to relax the tolerances of the assembly [20]. The stainless-steel box presses the cable over the copper sole, thus reducing the void fraction of the cable from the nominal value of 34% to about 20%. Inside the box, the Ni/Cr coating is removed from the strands at the cable terminations. The strands are soldered to the copper sole, thus reducing the overall electrical resistance of the joint [19, 20].

The safe operation of the joints is of great importance to guarantee adequate reliability and stability margin of the whole magnet. Several manufacturing techniques were recently proposed to improve the joint performance [21–23]. A low electrical resistance of the twin-box joint is required to assure low heating at the joint due to Joule effect during the magnet operation with transport current. In operation, the PF coils and their junctions are subjected to time varying magnetic fields, which induce eddy currents in the copper and in the stainless-steel parts of the joint and in addition coupling and hysteresis losses in the superconducting cables. The AC losses induced during electromagnetic transients can affect the thermal stability of the joint [24, 25].

The manufacturing process has a remarkable impact on the performance of the joint [26, 27]. Pre-qualification samples were fabricated for tuning the fabrication techniques and to build know-how for the manufacturing of the qualification samples. During the qualification phase, the manufacturing techniques and procedures were demonstrated as mature enough to guarantee a reliable performance of the joints. The qualification phase was completed in 2017 and successfully passed by the manufacturers, thus allowing to start the production phase [20]. Three different suppliers have been involved in the manufacturing of the PF coils for the ITER tokamak, from the European Union, the Russian Federation and China.

Detailed experimental investigations are required to limit the risk of thermal runaways at these locations during the magnet operation [28–30]. On this effort, several experimental campaigns were performed in the SULTAN test facility in Villigen, Switzerland [31] to analyze the performance of the twin-box joints in both DC and AC conditions. The tests were performed with the twin-box joints assembled in the so called 'praying hands' configuration.

This work presents a complete summary of the results obtained during the tests performed on the PF full-size joint samples (PF-FSJSs) in the SULTAN facility during the three manufacturing phases. Seventeen joint samples are considered for this analysis, including the series of samples manufactured in the European Union and a further sample manufactured in the Russian Federation (named PFJRF2). These samples were tested from October 2016 to September 2021 in the SULTAN test facility of the Swiss Plasma Center (SPC) in Villigen, Switzerland [31]. The main manufacturing characteristics of the PF-joint samples presented in this work are summarized in table 1. The results of the DC resistance and AC loss tests are presented for different operating conditions. The DC resistances are shown as a function of the background DC magnetic field, orientation of the transport current (direct or reverse) and cyclic loading of the joint. The AC losses at the joint are presented at different frequencies and amplitudes of the applied AC field, both before and after the cyclic loading with electromagnetic cycles. The results here reported are the most complete archive of the joint performances under several working conditions and the tests confirm the reliability of the PF joints during the future tokamak operation.

A novel 3D FE model of the PF joint, developed for a better understanding and interpretation of the tests, is presented and compared to the experimental results and to a previously developed model of the joint based on a distributed parameter electrical circuit [32]. The 3D model is able to precisely compute the experimental DC resistances and AC losses with a reduced computational burden. Furthermore, it proves very useful for the interpretation and understanding of these data. In particular, the model allows one selecting the most appropriate location of the voltage taps to be adopted for the measurement of the joint resistances in the SULTAN facility.

2. Experimental setup

The SULTAN test facility allows for DC resistance and AC loss measurements on the ITER CICCs and joint samples [31].

The PF-FSJSs were manufactured to test the performance of the inter-pancake joints between identical conductors of the PF coils. In the sample, shown schematically in figure 1, the two NbTi cables are electrically connected by a twin box joint realized in the 'praying hands' configuration. The joint is centered in the middle of the high field zone (HFZ) of the SULTAN facility.

2.1. Working conditions of DC and AC tests

The DC tests were performed to determine the joint electrical resistance with a 0 T, 3 T or 5 T background field. In the tests, the transport current was raised in steps from 0 to 55 kA in normal or reverse polarity.

During the AC tests, the AC losses in the joint were measured at 4.5 K, with a background magnetic field B_{DC} set to 3 T and applied along the x direction (see figure 1), both with and without transport current in the sample (from 0 to 55 kA). In these tests, the AC coils of the SULTAN facility were excited with a sinusoidal current, with a peak value of 230 A and 115 A, and a variable frequency in the range from 0.01 Hz to 1 Hz. The AC coils generate a sinusoidal magnetic field B_{AC} in the y direction (orthogonal to the DC field), with amplitude set to either 0.2 T or 0.1 T at the center of the SULTAN HFZ.

Table 1. Characteristics of PF-joint samples.

Sample	Cable type	# SC strands	Cu/nonCu strands	Jacket 316 l [mm]	Ni/Cr removal method	Resistivity		Shim thickness [mm]	Manufacturing phase	Notes
						Sole [nΩ m]	Shim [nΩ m]			
PFJEU1	PF6	1440	1.6	53.8 × 53.8	Reverse plating	2.74	0.155	1.8	Pre-Qualification	
PFJEU2	PF5	1152	2.3	51.9 × 51.9	Brush	4.55	0.43	7.0	Pre-Qualification	This sample has a defect in the soldered interface. This resulted in higher resistance.
PFJEU3	PF5	1152	2.3	51.9 × 51.9	Brush	4.55	0.43	7.0	Pre-Qualification	The central cooling pipe in PFJEU2 and PFJEU3 was with id = 6 mm. All other samples have id = 3 mm.
PFJEU5	PF6	1440	1.6	53.8 × 53.8	Reverse plating	2.75	2.75	3.9	Qualification	
PFJEU6	PF5	1152	2.3	51.9 × 51.9	Brush	3.34	3.34	7.1	Qualification	
PFJEU7	PF2,3,4	720	2.3	51.9 × 51.9	Brush	3.34	3.34	7.0	Qualification	
PFJRF2	PF1	1440	1.6	53.8 × 53.8	Brush	3.51	3.51	5.0	Qualification	Manufactured by RFDA, although PF1 and PF6 is the same conductor.
PFJEU8	PF6	1440	1.6	53.8 × 53.8	Reverse plating	3.14	3.14	7.0	Production	1st production sample of ASIPP
PFJEU9	PF5	1152	2.3	51.9 × 51.9	Brush	3.34	*	7.0	Production	*The shim was accidently made of OFE copper instead of DHP copper. The resistivity is unknown.
PFJEU10	PF6	1440	1.6	53.8 × 53.8	Reverse plating	3.14	3.14	7.0	Production	2nd production sample of ASIPP
PFJEU11	PF5	1152	2.3	51.9 × 51.9	Brush	3.34	3.34	7.1	Production	
PFJEU12	PF5	1152	2.3	51.9 × 51.9	Brush	3.34	3.34	7.1	Production	
PFJEU13	PF5	1152	2.3	51.9 × 51.9	Brush	3.34	3.34	7.1	Production	
PFJEU14	PF5	1152	2.3	51.9 × 51.9	Brush	3.34	3.34	7.1	Production	Same legs as in PFJEU12 but with the indium interface between them, and heat treated at 80 °C for 120 h to mimic the effect of the insulation curing.
PFJEU15	PF2,3,4	720	2.3	51.9 × 51.9	Brush	3.34	3.34	7.1	Production	
PFJEU16	PF2,3,4	720	2.3	51.9 × 51.9	Brush	3.34	3.34	7.1	Production	
PFJEU17	PF2,3,4	720	2.3	51.9 × 51.9	Brush	3.34	3.34	7.1	Production	Sample made of PFJEU16 legs. On one of the leg, a joint box is removed and replaced with a new one. This is done to qualify a repair procedure. The second leg remained original PFJEU16 leg.

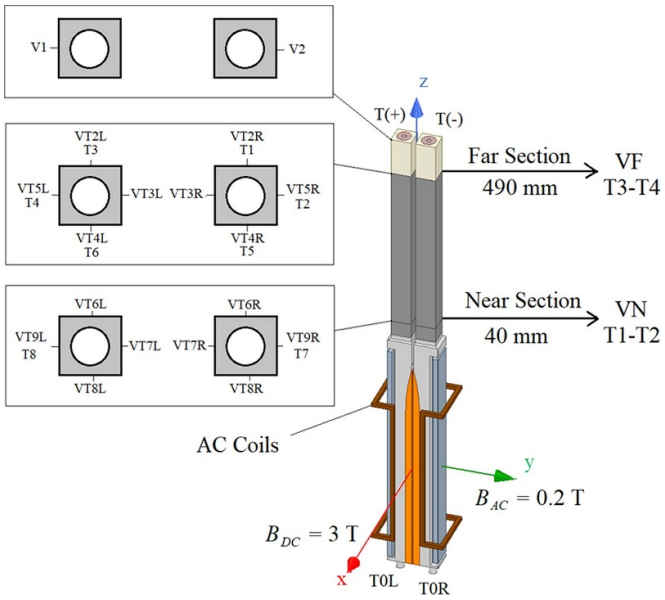

Figure 1. Experimental setup for DC resistance and AC loss evaluation of the PF-joint sample in the SULTAN test facility.

During the test campaign, the samples PFJEU10, PFJEU13, PFJEU14, PFJEU15, PFJEU16 and PFJEU17 were also tested with a background magnetic field $B_{DC} = 1$ T without transport current in the sample.

In the PFJRF2 sample, the impact on the joint performance of thermal cyclic loading—referred to as warm-up-cool-down (WUCD) applied after the electro-mechanical cyclic loading [33]—was also investigated. To this purpose, the AC losses in this sample were also measured after the WUCDs.

2.2. Instrumentation

The joint instrumentation consists of several sensors mounted along the sample, to measure voltage and temperature signals.

Two sets of voltage taps, positioned along the conductor jacket at different distances from the joint, are considered for the analysis: the first one is located at the outlet section of the joint (here referred to as *near section*, VN), while the second one is located at 450 mm (referred to as *far section*, VF) downstream of the outlet section of the joint. In order to take an average of the jacket voltage at each longitudinal position, four voltage taps are placed at each section. Voltage taps VT2 left/right, VT3L/R, VT4L/R and VT5L/R make up the voltage signal VF whereas VT6L/R, VT7L/R, VT8L/R and VT9L/R compose the voltage signal VN (figure 1). The positive terminal is located on top of the left leg, whereas the negative terminal is located on top of the right leg.

The temperature sensors T0L and T0R measure the inlet joint temperature, upstream of the HFZ. The downstream temperature is derived from the signals recorded at different distances from the joint: the set of signals T1 and T2 at the outlet section of the twin box joint and the set T3 and T4 at 450 mm downstream of the outlet section of the joint (figure 1). The temperature signals T1 and T2 are given by only one sensor each, named T8 and T7 respectively, whereas T3 and T4 refer to sets comprising three temperature sensors, named T3-T4-T6 and T1-T2-T5 respectively.

During the experiments, the joints are cooled down to 4.5 K, below the critical temperature of the NbTi strands of the PF conductors, in order to reach the superconducting state. The temperature and the pressure of the helium are measured upstream and downstream of the HFZ, where the joint is located. The helium mass flow rate is measured downstream of the HFZ through a flow-meter [17].

3. Procedures for the DC resistance and AC losses assessment

3.1. Procedure for the DC electrical resistance assessment

Two different assessments of the DC joint electrical resistance R_{joint} are performed in this study, by using the voltage signals VN and VF.

During the DC resistance tests, the transport current in the sample is increased in steps from 0 to 55 kA. The voltage V_i is the average value of the four voltage signals measured either at the *near* or at the *far* sections of the sample at the ith current step, with a current value I_i. The DC resistance is evaluated at each step of the transport current by applying the Ohm's law (voltmetric method).

The reference value of the DC resistance at a given working condition of the joint under test is the value computed at 55 kA transport current, since this is the nominal operating current and in addition, at high current values the relative measurement error is lower than at low currents.

3.2. Procedure for the AC losses assessment

The AC loss analysis is performed through the calorimetric method, i.e. by determining the helium enthalpy variation from upstream to downstream of the joint. In most cases, no adequate mixing of the heated helium is obtained next to the joint outlet (*near section*), due to the presence of a plug in the central cooling channel at the joint, which forces the helium to only flow in the conductor annular area in the region of the joint. The calorimetric assessment is therefore performed by using only the temperature signals T3 and T4 acquired 450 mm downstream the outlet of the joint (*far section*), where the helium temperature is more uniform in the conductor cross section and the temperature measured on the jacket can be considered as more representative of the helium temperature.

The power delivered to the helium is computed for the ith temperature sensor according to (1) for the left leg and to (2) for the right leg:

$$P_{\text{L}i} = \dot{m}_{\text{HeL}} \left(h_{\text{He}} \left(T_{3i}, P_{\text{outL}} \right) - h_{\text{He}} \left(T_{0\text{L}}, P_{\text{inL}} \right) \right) - P_{\text{offset},i} \quad (1)$$

$$P_{\text{R}i} = \dot{m}_{\text{HeR}} \left(h_{\text{He}} \left(T_{4i}, P_{\text{outR}} \right) - h_{\text{He}} \left(T_{0\text{R}}, P_{\text{inR}} \right) \right) - P_{\text{offset},i}. \quad (2)$$

The power offset ($P_{\text{offset},i}$) is computed as the average power found considering each temperature sensor before the external AC pulse and it is found to be strictly dependent on the helium mass flow rate in the corresponding leg. The power dissipated during the experiment is measured by considering the *i*th temperature sensor in each leg.

An example of the power measured during the tests of the PFJEU11 by the sensors T3, T4 and T6 of the left leg, referred as T_{3i} in (1), is shown in figure 2. After the offset subtraction, the power is integrated in time and the value of the *i*th energy is obtained.

The energy values are computed by considering all temperature sensors of T3 and T4. If the energy computed by a given temperature sensor shows a large difference (above 20%) with respect to the average energy computed by the remaining sensors of the same leg, it is discarded. The total energy dissipated in the sample is divided by the number of cycles of the AC pulse. The energy loss per cycle as a function of frequency is reported in this study for each PF-FSJS at different operating conditions with the corresponding error bars.

4. DC test results

4.1. DC electrical resistance at 0 T, 3 T and 5 T background field

The DC resistances of the PF-joint samples—estimated at different background field, with an operating current of 55 kA and considering the voltage signals acquired at the near and at the far section (450 mm from the joint)—are summarized in figures 3 and 4 respectively.

The resistances found at the far section exhibit higher values, up to a factor 2 for the samples PFJEU9 and PFJEU11, than the results measured at the near section. This difference could be due to the current distribution imbalance in the region nearby the joint. A possible explanation is that in the joint region some strands are in better contact with the Cu saddle compared to other strands deeper in the cable. Some of the strands are therefore overloaded with current, while others carry only a fraction of current. In the cable region adjacent to the joint, the current redistributes from the overloaded strands to the other ones, thus affecting the measurement at the *near* location. The most reliable values of the DC resistances are those obtained from the *far* voltage signals, as will be later discussed. Therefore, the signal VF is used as a reference for the evaluation of R_{joint}. The 3D FEM model confirms that the *far* section sensor is more reliable than the *near* section one.

The impact of the magnetic flux density on the joint resistance is shown in figure 4. When the field increases from 0 T to 5 T, all samples, except for PFJEU2 and PFJEU3 (pre-qualification samples), exhibit an increase of the DC resistance below 30%. The resistances of these samples show a greater dependence on the magnetic field compared to other samples (see figure 4). This can be attributed to the low resistive shims in these two samples (see their RRR values in table 1), whose magnetoresistance effect is not negligible and thus affects the total resistance of the joint.

It is worth noting in figure 4 that the production samples exhibit a lower average resistance than the qualification samples, which indicates that the quality of the manufacturing procedures was maintained, or even improved, throughout the production phase. Some differences between the pre-qualification and the following samples can also be justified by the difficulty, in the early phases of manufacturing, to keep the nominal twist pitch while inserting the cable into the stainless-steel box. In some cases, the end of the cable (about 100 mm) was untwisted, which could result in a higher void fraction and possible movements of the strands under the application of the Lorentz force.

4.2. Impact of current direction on DC electrical resistance

The DC resistances of the PF joint were measured during the tests with either normal or reverse polarity of the current in the joint, corresponding to +55 and −55 kA respectively.

In case of normal polarity, the current flows from the positive terminal to the negative one, see figure 1. In this case, the combination of background field and direct transport current in the joint results in a repulsive Lorentz force between the two conductors at the boxes. In case of reverse polarity, the combination of background field and reverse transport current acts as an attractive force on the boxes.

In figure 5, the results are shown for the pre-qualification, qualification and production samples. Most of the samples exhibit a negligible variation (below 3%) of the resistance for reverse polarity. In two cases, for the samples PFJEU3 and PFJEU9, a somewhat greater variation (about 10%) of the resistance is found.

These results in general show that the repulsive or attractive Lorentz forces acting between the conductors at the joint have a negligible impact on the DC resistance of the joints.

4.3. Impact of EM cycles on DC electrical resistance

The impact of EM cycles [33] on the joint resistances is shown in figure 6. The results presented are obtained by considering the voltage signals acquired at the far sections, with an operating current of 55 kA and a background field of 3 T.

4.3.1. Impact of EM cycles on DC electrical resistance of the pre-qualification and qualification samples. As shown in figure 6, the qualification samples exhibit a negligible variation of resistance with EM cycles.

The resistances of the PFJEU6, assembled with PF5 cables, exhibit a variation of about 4% while the resistance of the PFJEU1, a pre-qualification sample assembled with PF6 cables, does not exhibit any significant variation with cyclic loading.

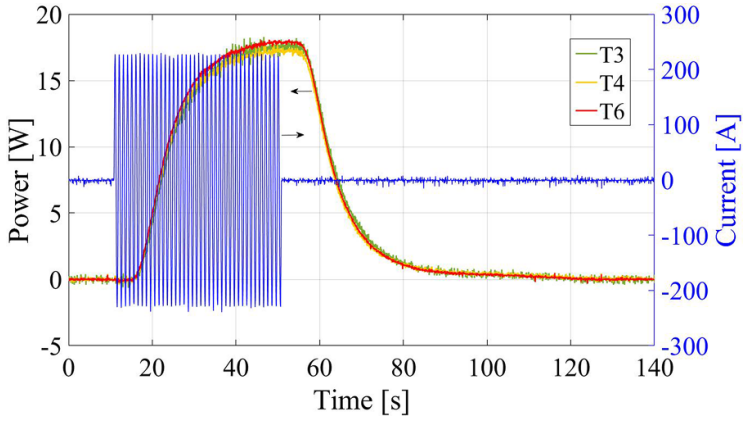

Figure 2. Evolution in time of the power measured by the sensors T3, T4 and T6 of the left leg during the tests of the sample PFJEU11. On the right axis, the sinusoidal variation of the current in the AC coils.

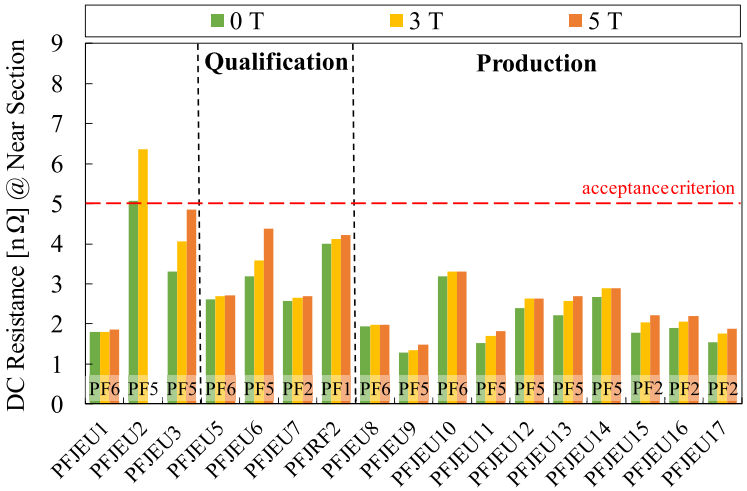

Figure 3. Summary of the DC resistances before EM cycling on the PF-joint samples considering voltage signals acquired at the near section with an operating current of 55 kA (the sample PFJEU2 was not measured at 55 kA and 5 T).

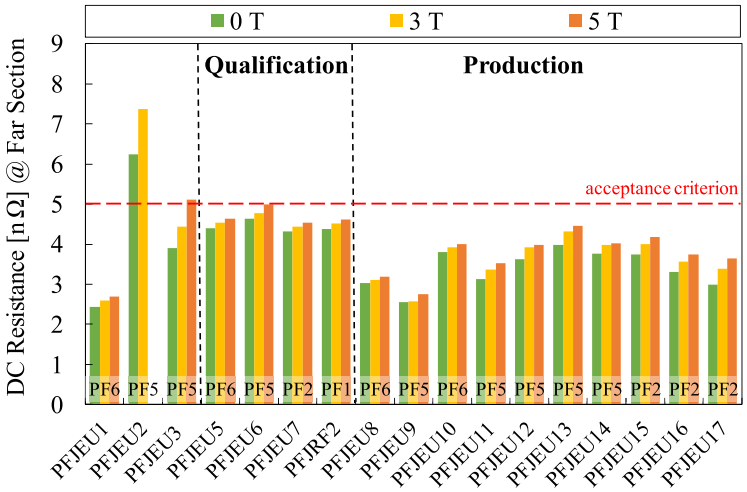

Figure 4. Summary of the DC resistances before EM cycling on the PF-joint samples considering voltage signals acquired at the far section with an operating current of 55 kA (the sample PFJEU2 was not measured at 55 kA and 5 T).

The PFJEU2 sample, based on PF5 cables, exhibits a DC resistance value exceeding the 5 nΩ acceptance criterion and its value increases by about 15% after 1000 EM cycles. A post-mortem examination was performed on this particular sample to better understand its poor electrical performance. Cutting the joint into sections revealed that the soldering

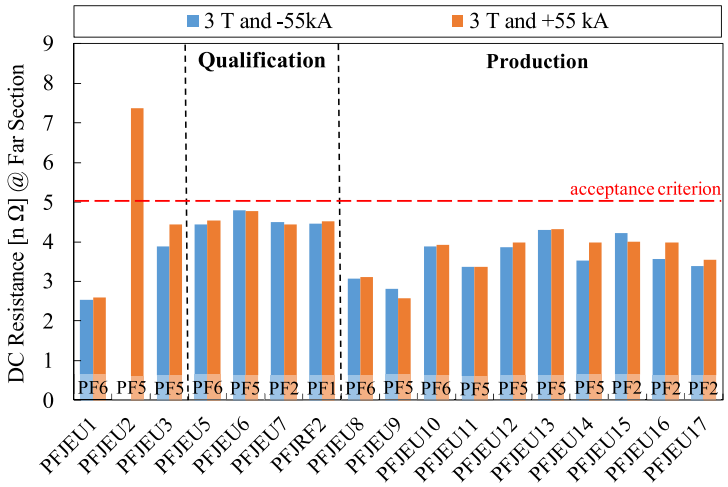

Figure 5. Summary of the DC resistance before EM cycling on the PF-joint samples considering voltage signals acquired at the far section with an operating current of +55 kA and −55 kA (the sample PFJEU2 was not measured at −55 kA and 3 T).

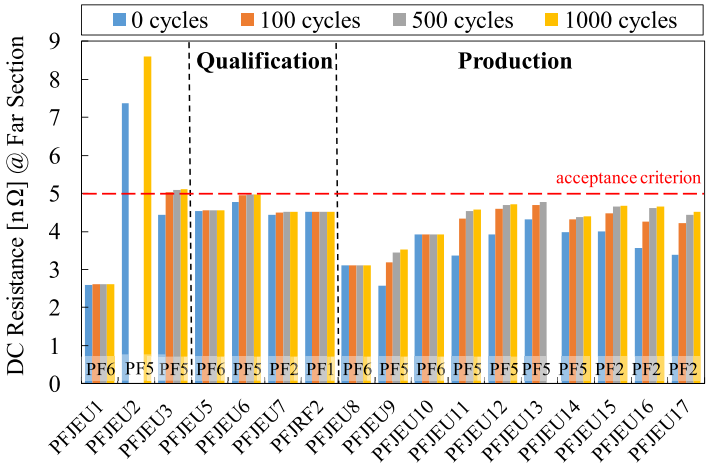

Figure 6. Impact of EM cycles on the DC resistance of PF-joint samples considering voltage signals acquired at the far section with an operating current of 55 kA and background field of 3 T (the sample PFJEU2 was not measured after 100 and 500 EM cycles).

between the boxes and the shim was poor, so that the various parts disintegrated without any effort when the steel structure around the joints was removed. The poor soldering was identified as the source of this particularly high joint resistance.

4.3.2. Impact of EM cycles on DC electrical resistance of the production samples. The resistances of the PFJEU8 and PFJEU10 samples, both assembled in the production phase with PF6 cables, do not exhibit any significant variation with EM cycles.

The resistance of the PFJEU12, assembled with PF5 cables, increases from 3.9 nΩ before cyclic loading to 4.6 nΩ after 100 EM cycles, corresponding to an increase of 17%, and to 4.7 nΩ, after 1000 EM cycles, corresponding to a global increase of about 20%.

For the PF5-based joints, the resistance increases quite significantly, up to 36%. Most of the increase is observed in the first 100 EM cycles. The DC resistance of the PFJEU13 sample was not measured after 1000 EM cycles.

5. AC loss test results

5.1. AC losses without transport current

5.1.1. AC losses without transport current in the pre-qualification and qualification samples. Measurements at $B_{DC} = 3$ T, $B_{AC} = \pm 0.1$ T. The energy losses per cycle versus frequency are summarized in figure 7 for pre-qualification and qualification samples with a background field of 3 T, no transport current in the sample and pulsed field $B_{AC} = \pm 0.2$ T.

The energy losses per cycle of the qualification samples are almost constant with a pulsed field of ±0.2 T for frequencies between 0.2 Hz and 0.4 Hz, with a saturation value between 30 J cyc^{-1} and 40 J cyc^{-1}.

The PFJRF2 sample, assembled with PF1 cables, exhibits a local peak of loss at 0.1 Hz, so that the highest losses are found at a lower frequency than in the other samples.

Measurements at $B_{DC} = 3$ T, $B_{AC} = \pm 0.1$ T. The losses were also measured at $B_{AC} = \pm 0.1$ T for the samples PFJEU2, PFJEU3, PFJEU6 and PFJEU7. The corresponding results of

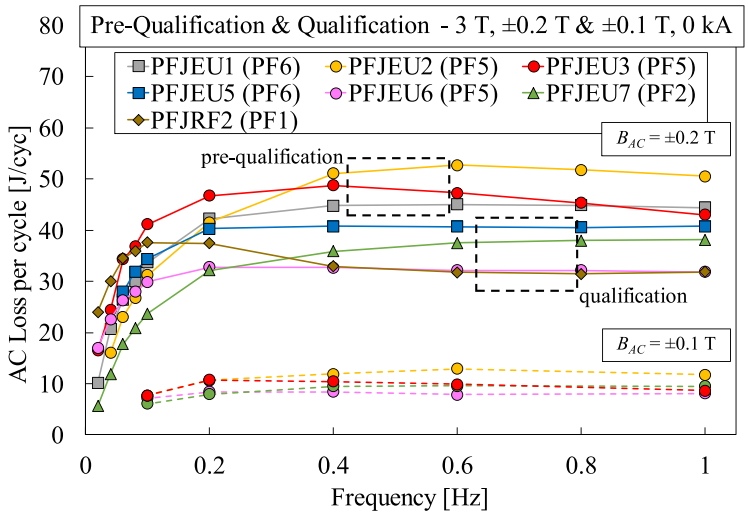

Figure 7. Energy loss per cycle after EM cycling of the pre-qualification and qualification PF-joint samples with 0 kA transport current, 3 T background DC field, ±0.2 T and ±0.1 T AC field.

these samples are added in figure 7. The loss vs frequency curves exhibit a saturation around 0.2 Hz. At frequencies above 0.2 Hz, the losses are about one-fourth of those found at $B_{AC} = \pm 0.2$ T, as expected from their theoretical dependence on the square of the field amplitude.

5.1.2. AC losses without transport current in the production samples. Measurements at $B_{DC} = 3$ T, $B_{AC} = \pm 0.2$ T. In figures 8(a)–(d), the curves of energy loss per cycle versus frequency are shown for the production samples with a background field of 3 T, no transport current in the sample and pulsed field B_{AC} of ±0.2 T and ±0.1 T. Figure 8(a) shows the results of the samples assembled with PF5 cables, while figure 8(b) reports the results of joints between PF6 cables and figure 8(c) the joints between PF2/3/4 cables.

At $B_{AC} = \pm 0.2$ T, the sample assembled with PF5 and PF6 cables exhibits losses at saturation in the range of 35–40 J cyc^{-1}, while 10% higher values are observed for most of the samples assembled with PF2 cables, which are characterized by a lower number of strands (720).

The samples PFJEU8 and PFJEU9, based on PF6 and PF5 cables respectively, are characterized by a different profile of the AC loss curve with respect to the other production samples, since no saturation is observed.

The PFJEU8 sample exhibits an energy loss per cycle which monotonously increases with frequency. At 1 Hz, the PFJEU8 exhibits about 25% higher losses than the other samples at the same frequency.

The sample PFJEU9 exhibits losses per cycle higher than the other samples between 0 and 0.6 Hz. This peculiar behavior can be explained by considering that the shim of the PFJEU9 sample was accidently made of oxygen-free (OFE) copper instead of deoxidized (DHP) copper. This sample is therefore characterized by a lower copper resistivity than the other samples, which determines its different behavior.

The impact of the indium interface was investigated on the sample PFJEU14. This sample was assembled with the same conductors of the PFJEU12 sample but with an indium interface in between. The results demonstrate that this interface has no large impact on the losses (about 10%).

During this campaign, the procedure to repair a joint after damage was tested on the sample PFJEU17. The box of PFJEU16 was removed and one leg was replaced. The sample was then measured as PFJEU17. After repairing, no significant variations of the losses were observed.

Measurements at $B_{DC} = 3$ T, $B_{AC} = \pm 0.1$ T. With the exception of sample PFJEU10, the production joints were tested at $B_{AC} = \pm 0.1$ T, see figures 8(a)–(c). As previously described for the pre-qualification and qualification samples, also the production samples exhibit some saturation at 0.3 Hz. Above 0.3 Hz, the losses at $B_{AC} = \pm 0.1$ T are about one-fourth of those with $B_{AC} = \pm 0.2$ T, consistently with the analytical formulae.

Also in these working conditions, the sample PFJEU9 exhibits a different loss curve with respect to the other samples (see figure 8(a)). As already mentioned, this sample was manufactured with a low resistive shim, which explains its different behavior.

Measurements at $B_{DC} = 1$ T, $B_{AC} = \pm 0.2$ T. The samples PFJEU10, PFJEU13, PFJEU14, PFJEU15, PFJEU16 and PFJEU17 were tested also at a lower background field $B_{DC} = 1$ T. For the sake of simplicity, the results at lower background field are added in figure 8(d) for two selected samples (PFJEU10 and PFJEU14). A similar profile can also be observed for the other samples (not reported in figure 8(d)). At 0.8 Hz, the losses at $B_{DC} = 1$ T are 30% higher than those found at $B_{DC} = 3$ T.

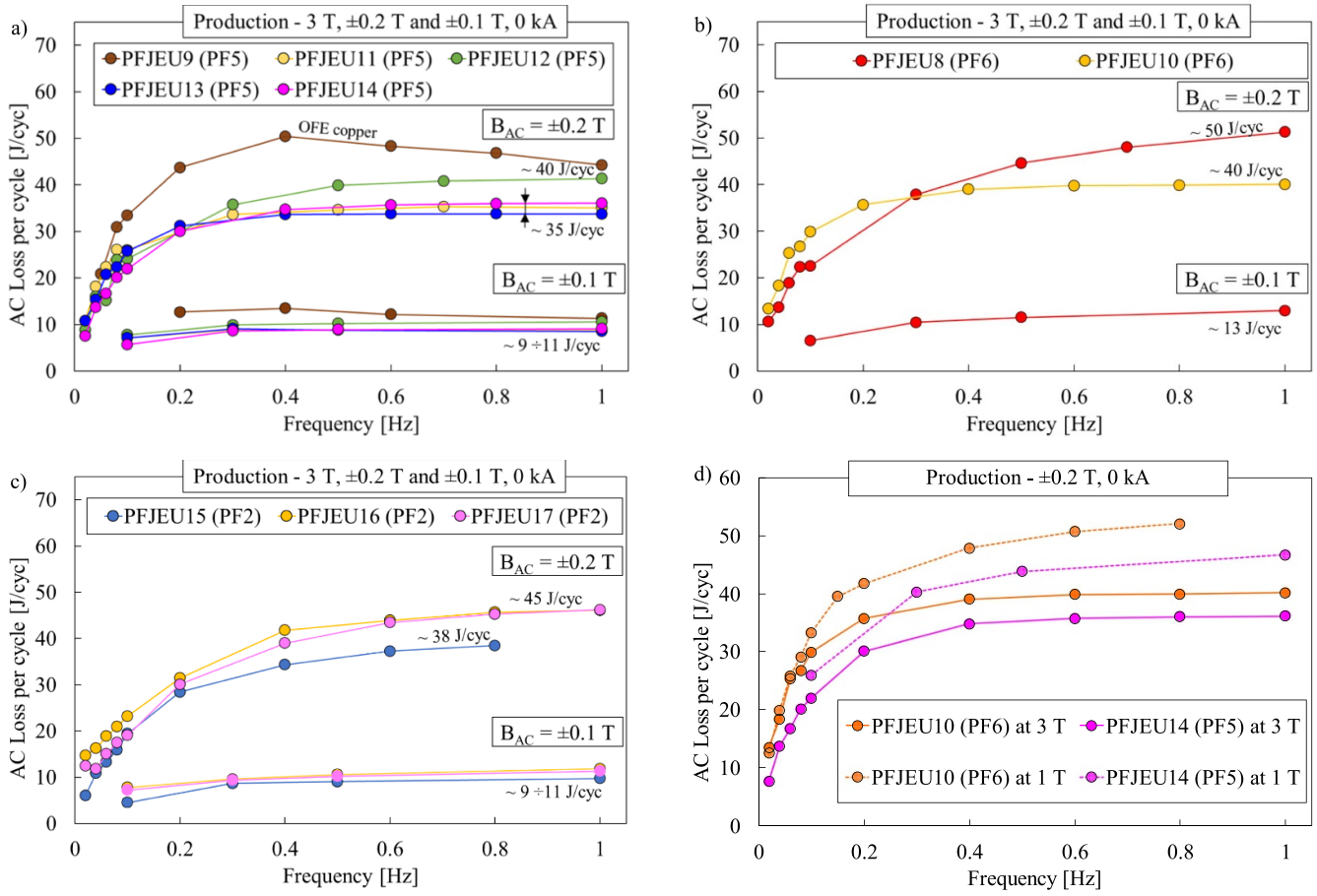

Figure 8. Energy loss per cycle after EM cycling of the production PF-joint samples with 0 kA transport current, (a) 3 T background DC field, ±0.2 T and ±0.1 T AC field (joint assembled with PF5 cable), (b) 3 T background DC field, ±0.2 T and ±0.1 T AC field (joint assembled with PF6 cable), (c) 3 T background DC field, ±0.2 T and ±0.1 T AC field (joint assembled with PF2/3/4 cable), (d) 1 T background DC field, ±0.2 T AC field.

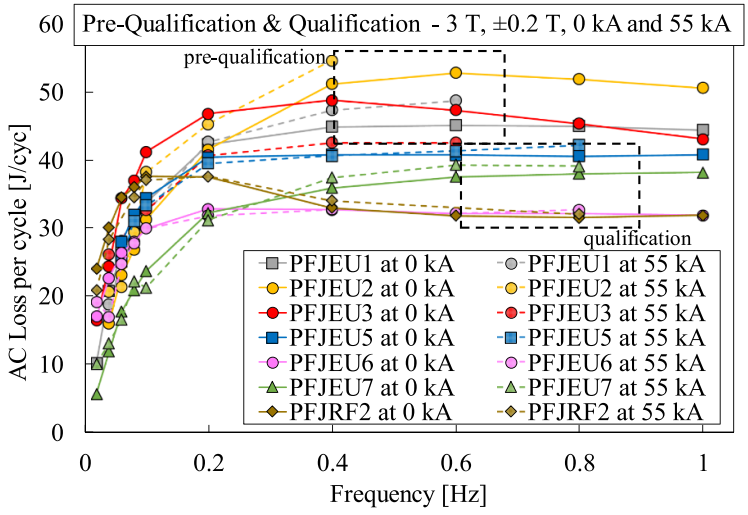

Figure 9. Energy loss per cycle after EM cycling of the pre-qualification and qualification PF-joint samples with 3 T background DC field, ±0.2 T AC field, 0 kA and 55 kA transport current.

5.2. AC losses with 55 kA transport current

Measurements at B_{DC} = 3 T, B_{AC} = ±0.2 T. During the test campaign, the impact of the transport current on AC losses was analyzed. In figure 9, the curves of energy loss per cycle—obtained with a background field of 3 T, pulsed field of ±0.2 T and 55 kA transport current in the samples—are shown for the pre-qualification and qualification samples.

These results are compared with the losses measured without transport current.

The qualification samples generally exhibit an increase of losses due to transport current within 5%. The effect of the transport current on the pre-qualification samples is greater than on the qualification samples, but still limited within the error margin.

Even though not reported in the plots, also the losses in the production samples only exhibit a slight variation with transport current, limited below 12%.

These results show that the transport current does not affect significantly the AC losses of the pre-qualification and qualification samples. This indicates that the Lorentz force variation between these two working conditions does not significantly modify the interstrand conductances.

5.3. Impact of thermal cycle on AC losses

During a thermal cycle (WUCD), the samples are warmed up to room temperature and then cooled down to supercritical helium temperature. This procedure, which will necessarily be applied during the operation of the ITER machine, might affect the joint performance. The impact of WUCDs on losses was therefore investigated during the tests of the qualification sample PFJRF2, assembled with PF1 cables [29, 30].

In figure 10, the losses vs frequency curves of PFJRF2 are shown with a background field of 3 T, no transport current in the sample and pulsed field amplitudes set to ± 0.2 T and ± 0.1 T.

Comparing the results obtained before and after the thermal cycles shows that the impact of WUCDs on losses is negligible. At 0.1 Hz, the losses increase by about 4% after two thermal cycles while at 0.8 Hz, the increase is limited below 1%. Similar results are observed even at $B_{AC} = \pm 0.1$ T.

6. 3D FEM model of the PFJEU13

A model of a selected sample, PFJEU13, was implemented in a 3D FEM code suitable for the analysis of electromagnetic problems [34].

The joints are modeled with their stainless steel structure, as shown in figure 11(a). The stainless steel structure was retained in the model in the first simulations, in order to assess its impact on the DC resistances and AC losses of the joint. After observing that, the presence of the stainless steel does not affect the results, the model of the joint was simplified by retaining only the NbTi cables and the copper parts, as shown in figure 11(b). Figure 11(b) also shows the AC coils of the SULTAN facility used for the application of the AC field.

6.1. Model description

In the model, no twisted cabling layout was considered. The two cables were described through a homogeneous anisotropic medium, with a very high conductivity along the axis of the cable (the z axis of the SULTAN facility), named C_l, and a lower value of conductance in the transverse direction (on the x-y plane orthogonal to the z-axis), named C_t.

The dimensions of the joint and the materials resistivities were provided by a post-mortem inspection performed at CERN [27].

6.2. AC losses calculation

The AC loss vs. frequency profile is estimated by the model with a background field of 1 T. The transverse and longitudinal conductivities of the NbTi cables are set to $C_t = 2.5 \times 10^7$ S m^{-1} and $C_l = 5.0 \times 10^{14}$ S m^{-1}. The copper resistivity in the shim and soles is set to 3.37 nΩ m, corresponding to the measurement performed at 1 T background field [27]. The results of the AC loss calculations performed with this model are shown in figure 12. The losses are computed even at frequencies below 0.1 Hz, for which no experimental data are available.

To validate the accuracy of the 3D FEM model, the losses are compared with the measured values and with the results found with a previously developed model of the PF-joint based on a distributed 3D non-linear circuit [32, 35]. The results of the models and the measurements exhibit a difference below 10% (with the exception of the loss at 0.1 Hz). The losses computed by the two models exhibit a difference at low frequencies probably due to the different level of discretization. In the THELMA code, the cables are discretized at the last-but one cabling stage while in the 3D FEM the cabling layout is not modeled. The 3D FE model well reproduces the saturation of the losses observed in the experiments above 0.5 Hz.

6.3. DC resistance calculation

The DC resistance of the cable in the 'praying hands' configuration is computed by setting the voltage at the upper terminal of one cable to a given value to 100 μV and the upper terminal of the other cable to 0 V. An example of voltage and current distribution in the joint is shown in figure 13.

The DC resistance was determined with two computation methods, referred to here as the *voltmetric method* and the *calorimetric method*.

For the *voltmetric method*, the total current flowing in the joint with a given applied voltage is obtained by integrating the computed current density over the cross section of the conductor. To check the consistency of the model, the total current is also computed by integrating the current density over three transverse cross sections, namely the cross section of the right leg conductor, the cross section of the left leg conductor and the middle plane of the joint (located inside the copper saddle). No significant differences are found between these three approaches. The joint DC resistance R_{DC} is then simply computed as:

$$R_{DC} = \frac{\Delta V}{I}. \tag{3}$$

In the *calorimetric method*, the DC resistance was estimated by computing the total joule power deposited in the joint

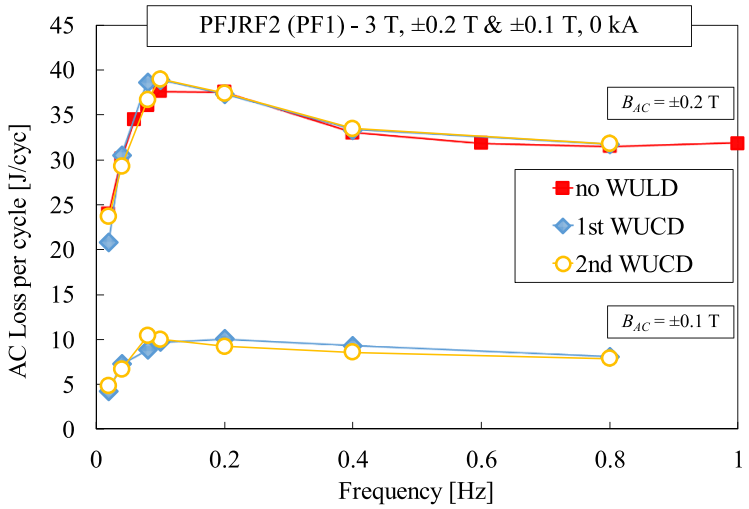

Figure 10. Energy loss per cycle of the qualification sample PFJRF2 after two thermal cycles with 0 kA transport current, 3 T background DC field, ±0.2 T and ±0.1 T AC field.

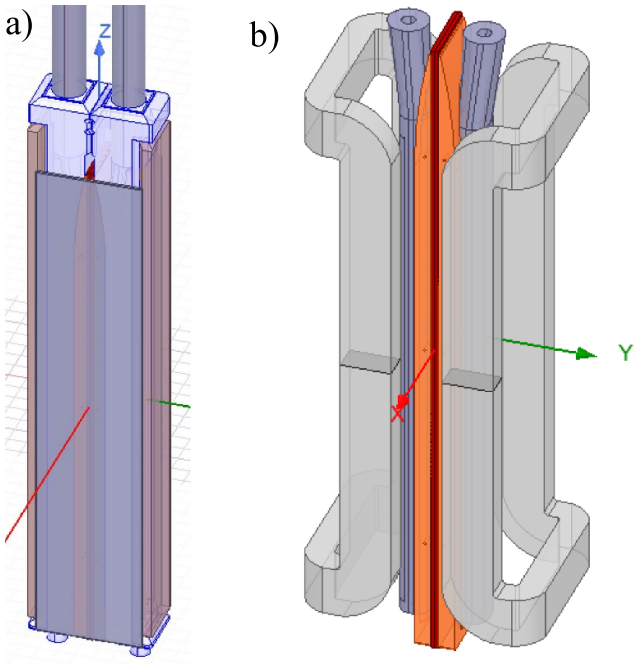

Figure 11. 3D FEM Full Model of the PFJEU13 for the DC Resistance computation. (a) Full joint model including the stainless-steel structure and (b) simplified model of the joint with copper saddles, copper shim, and NbTi cables, also showing the AC coils of the SULTAN facility.

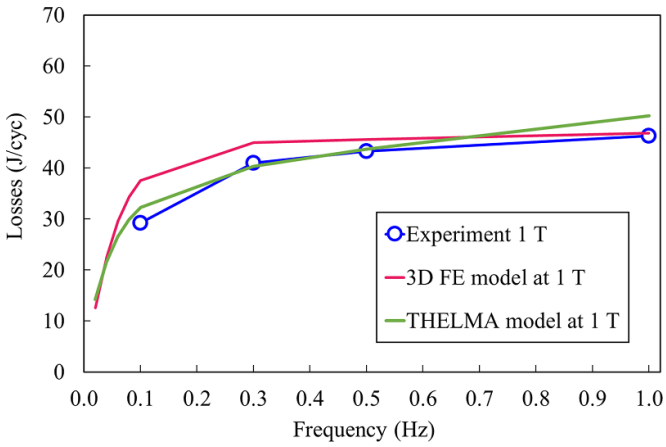

Figure 12. Comparison of the AC loss profiles of the experimental results and the numerical results at 1 T.

Table 2. DC Resistances.

Model voltmetric method 3 T	Model calorimetric method 3 T	Experiment 3 T
4.77 nΩ (with cables) 3.57 nΩ (with/o cables)	4.77 nΩ (with cables) 3.57 nΩ (with/o cables)	4.30 nΩ

during the virtual measurement:

$$R_{\mathrm{DC}} = \frac{\Delta V^2}{\int_\tau (E \cdot J)\, \mathrm{d}\tau} \tag{4}$$

where the volume τ includes both the copper part and the NbTi cables.

A separate assessment of the DC resistance was performed without the superconducting cables, i.e. removing the cables from the model. The DC resistance was computed by applying the *voltmetric* and the *calorimetric* methods, with and without the external stainless-steel box. In all cases, the result obtained is 3.57 nΩ, that confirms an excellent agreement between the *voltmetric* and *calorimetric* methods and the negligible impact of the stainless-steel structure.

In table 2, the computed (with and with/o the cables in the model) and measured values of the DC resistances at 3 T background field are compared. A difference of about 10% is found between the computed and measured values.

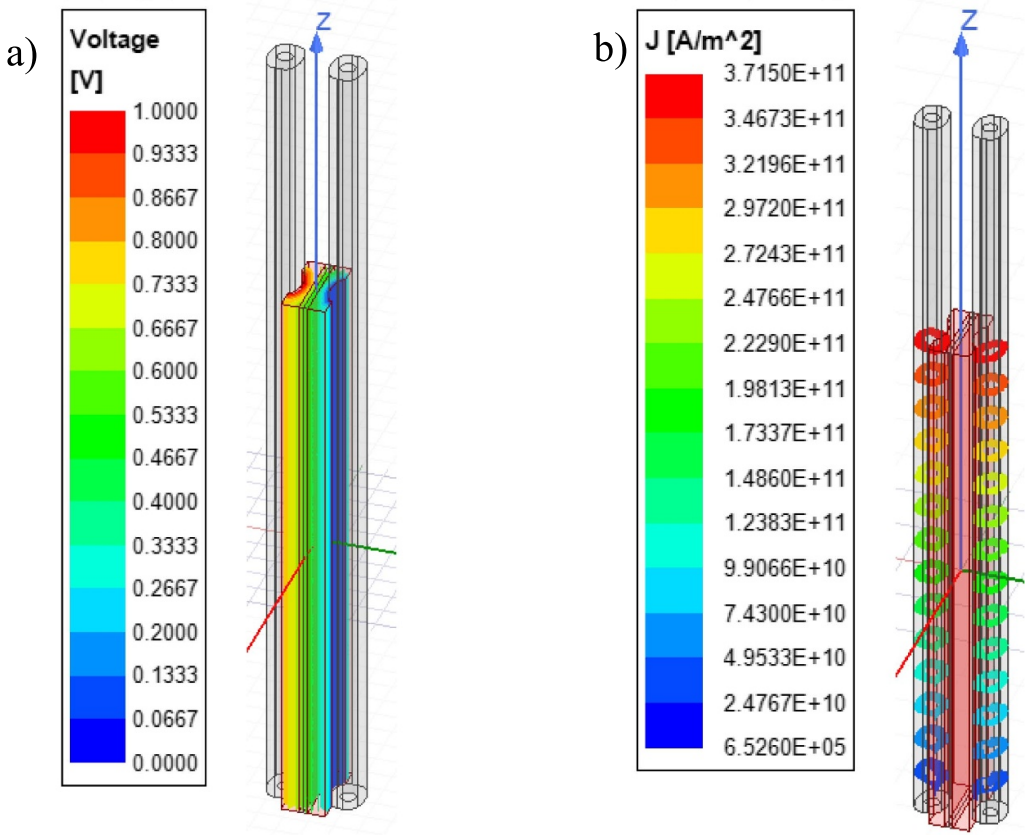

Figure 13. (a) Voltage and (b) current distribution during a simulation of the DC resistance measurement.

It is worth mentioning that the DC resistance was not measured at a background field of 1 T, while experimental values of AC losses are available in these conditions. Therefore, a direct comparison of the calculations and the measurements of the DC resistances at 1 T is not possible.

The DC results are relevant for a better interpretation of the experimental data. As shown in figures 3 and 4, during the tests, the voltage taps located *near* the joint measure a DC joint resistance of about 2.5 nΩ, while the voltage taps located *far* from the joint measure a value of about 4.3 nΩ at 3 T. The resistance due to the copper part of the joint, computed equal to 3.57 nΩ, should always be lower than the total resistance of the joint itself.

The calculations therefore indicate that the most accurate measurement of the joint resistance is the one retrieved from the voltage taps located *far* from the joint, for which the measured resistance is higher than the contribution of the copper. This is not the case for the voltage taps located *near* the joint, which therefore seems to provide a non-accurate result.

7. Conclusions

This work presents a comprehensive review of the tests performed from 2016 to 2021 during the pre-qualification, qualification and production phase of the superconducting twin-box joints for the PF coils of the ITER magnet system. This work builds up a large database of the losses during electrodynamic transients and of the electrical resistances in DC conditions. These data demonstrate the reliability of the joint manufacturing and confirm the compliance of the joint performance to the design criteria. The results are suited for the prediction of the joint behavior during the tokamak operation and can be furthermore adopted for the validation of numerical or analytical models aimed at a better understanding of the dependence of joint resistances and losses on the main joint parameters.

All samples tested during the qualification and production phases meet the 5 nΩ at 5 T acceptance criterion for the DC resistance, which demonstrate that the joint manufacturing procedures set in the pre-qualification phase are robust and well suited for the industrial production.

The measurements show the moderate impact of the background field on the DC electrical resistance: the resistance increases by less than 10% with the background field increasing from 0 T to 5 T. The largest variations were found for the samples manufactured with shims characterized by a high RRR, whose magnetoresistance affects the overall joint resistance.

The qualification samples exhibit a higher average DC resistance than the production samples, which shows that a good quality of manufacturing was maintained throughout the production phase.

The impact of electromagnetic cycles on the DC electrical resistances was investigated by performing measurements in virgin conditions and after 100, 500 and 1000 EM cycles. The results show an increase of resistance with cyclic loading up to 36%. The largest resistance variation is observed during the first 100 EM cycles. In all samples a saturation is observed at about 1000 cycles and occurs at values below the acceptance criterion.

During the test campaign, the electrodynamic losses were measured with a background field of 3 T, no transport current in the sample and with a sinusoidal field of ± 0.2 T and ± 0.1 T in a range of frequencies up to 1 Hz.

With a sinusoidal field of ± 0.2 T, all samples exhibit a saturation of the losses per cycle for frequencies above 0.4 Hz. The energy losses per cycle reach a saturation value between 40 J cyc^{-1} and 50 J cyc^{-1} for the pre-qualification samples and between 30 J cyc^{-1} and 45 J cyc^{-1} for the qualification and production samples.

The joints were studied at different working conditions during the test campaign. When the DC background field is changed from 3 T to 1 T, the losses increase by about 30%. The losses increase by (roughly) a factor 4 with increasing the AC field amplitude from 0.1 T to 0.2 T; this result confirms the theoretical dependence of the losses per cycle (both in the NbTi cables and in the copper of the saddle) on the square of the field amplitude.

The impact of the transport current on the measured AC loss vs frequency curves is negligible; this result indicates that the Lorentz force does not significantly affect the main joint electrical parameters, such as the strand-strand and the strand-copper sole contact resistances.

The impact of thermal cycles was assessed on the qualification sample PFJRF2, assembled with PF1 cables. The loss increment is below 5% after two thermal cycles, which indicates a negligible impact of the WUCDs on the losses at the joints.

A 3D FEM model was developed to analyze the AC losses and the DC resistances in the PF joint. Notwithstanding several simplifications, the model is able to compute both AC losses and DC resistances with an average error of about 10% with respect to the experimental data. The model represents a useful tool for interpreting the measurement results: the resistance—computed with the model—due to the copper part of the joint only is higher than the total resistance of the joint measured by the sensors located *near* the joint outlet. The sensors located *far* from the joint outlet (450 mm) measure instead resistance values greater than the contribution of the copper only. Since the overall joint resistance cannot be lower than the contribution of its copper part, we conclude that the sensors located at 450 mm from the joint outlet provide a more accurate measure of the DC resistance value.

The model provides an accurate calculation of the overall DC resistance and of the AC losses in the joint with an acceptable computational time and, further, it can be used to explore the joint losses under different magnetic field profiles for the simulation of the plasma scenarios.

Data availability statement

The data cannot be made publicly available upon publication due to legal restrictions preventing unrestricted public distribution. The data that support the findings of this study are available upon reasonable request from the authors.

Acknowledgments

Dr Bruzzone and the team of the SPC, Villigen, Switzerland are gratefully acknowledged for performing the experimental tests analyzed in this work. The work at the University of Bologna was supported by Contract IO/17/CT/4300001613 with the ITER Organization, France.

Disclaimer

The views and opinions expressed herein do not necessarily reflect those of the ITER Organization.

ORCID iDs

M Breschi https://orcid.org/0000-0001-9025-2487
L Cavallucci https://orcid.org/0000-0002-0096-4817
K Sedlak https://orcid.org/0000-0002-2090-1709

References

[1] Mitchell N, Devred A, Libeyre P, Lim B and Savary F 2012 The ITER magnets: design and construction status *IEEE Trans. Appl. Supercond.* **22** 4200809
[2] Mitchell N, Bessette D, Gallix R, Jong C, Knaster J, Libeyre P, Sborchia C and Simon F 2008 The ITER magnet system *IEEE Trans. Appl. Supercond.* **18** 435–40
[3] Devred A, Backbier I, Bessette D, Bevillard G, Gardner M, Jewell M, Mitchell N, Pong I and Vostner A 2012 Status of ITER conductor development and production *IEEE Trans. Appl. Supercond.* **22** 480–90
[4] Huguet M, Team I T E R J C and Teams I H 2001 Key engineering features of the ITER-FEAT magnet system and implications for the R&D program *Nucl. Fusion* **41** 1503–13
[5] Lim B, Simon F, Ilyin Y, Gung C Y, Smith J, Hsu Y H, Luongo C, Jong C and Mitchell N 2010 Design of the ITER PF coils *IEEE Trans. Appl. Supercond.* **21** 1918–21
[6] Lim B, Simon F, Ilin Y, Gung C Y, Boyer C, Beemsterboer C, Valente P, Lelekhov S and Mitchell N 2012 Development of the ITER PF coils *IEEE Trans. Appl. Supercond.* **22** 4201404
[7] Lim B *et al* 2016 Approaching ITER PF coil manufacturing *IEEE Trans. Appl. Supercond.* **26** 4205204
[8] Zanino R, Bagnasco M, Bellina F, Gislon P, Ribani P L and Richard L S 2005 Modeling AC losses in the ITER NbTi poloidal field full size joint sample (PF-FSJS) using the THELMA code *Fusion Eng. Des.* **75–79** 23–27
[9] Simon F 2010 Reliability considerations for the ITER poloidal field coils *IEEE Trans. Appl. Supercond.* **20** 423–6
[10] Ciazynski D, Duchateau J L, Decool P, Libeyre P and Turck B 2001 Large superconductors and joints for fusion magnets:

from conceptual design to testing at full scale *Nucl. Fusion* **41** 223–6
[11] Ciazynski D and Martinez A 2002 Electrical and thermal designs and analyses of joints for the ITER PF coils *IEEE Trans. Appl. Supercond.* **12** 538–42
[12] Decool P, Ciazynski D, Libeyre P, Della Corte A, Spadoni M, Rossi S, Laurenti A, Beaudet F, Bourquard A and Bresson D 2003 Design and manufacture of a prototype NbTi full-size joint sample for the ITER poloidal field coils *Fusion Eng. Des.* **66** 1165–9
[13] Zanino R *et al* 2005 Current distribution measurement on the ITER-type NbTi bus bar III *IEEE Trans. Appl. Supercond.* **15** 1407–10
[14] Simon F 2012 Design of the ITER PF coil joints *IEEE Trans. Appl. Supercond.* **22** 4804104
[15] Rolando G, van Lanen E, van Nugteren J, Offringa W, ten Kate H H J, Ilin Y, Lim B, Simon F and Nijhuis A 2013 Analysis of heat load, current margin and current non-uniformity in ITER PF coil joints *IEEE Trans. Appl. Supercond.* **23** 4201405
[16] Bellina F, Bettini P and Trevisan F 2004 Electromagnetic analysis of superconducting cables and joints in transient regime *IEEE Trans. Appl. Supercond.* **14** 1356–9
[17] Yao Y, Song Y T, Wu H, Huang X Y, Shen G, Hu B, Wang L and Zheng X D 2015 Design and analysis of full size joint sample for ITER PF coil *J. Fusion Energy* **34** 802–7
[18] Stepanov B *et al* 2015 Twin-box ITER joints under electromagnetic transient loads *Fusion Eng. Des.* **98–99** 4201305
[19] Ilyin Y *et al* 2016 Design and qualification of joints for ITER magnet busbar system *IEEE Trans. Appl. Supercond.* **26** 1–5
[20] Ilyin Y *et al* 2018 Qualification program of lap joints for ITER coils *IEEE Trans. Appl. Supercond.* **28** 1–6
[21] Zhang Q, Ito S and Hashizume H 2023 Bending and twisting characteristics of REBCO lap joint with indium *IEEE Trans. Appl. Supercond.* **33** 4201305
[22] Girard S *et al* 2023 SELFIE: ITER superconducting joint test facility *Fusion Eng. Des.* **188** 113434
[23] Xu Y, Lu K, Shen G, Hu B, Cheng F, Mo C, Zhang M and Xie Y 2023 Void fraction research and destructive examination of CFETR toroidal field coil protype joints *Ann. Nucl. Energy* **188** 109802
[24] Ilyin Y, Rolando G, Nijhuis A, Simon F, Lim B S, Mitchell N and Turck B 2014 Simulations of twin-box joints for ITER PF coils *IEEE Trans. Appl.Supercond.* **24** 9001905
[25] Ilyin Y, Rolando G, Turck B, Nijhuis A, Simon F, Lim B-S and Mitchell N 2016 Analysis of ITER PF coil joint design under reference operating scenario *IEEE Trans. Appl. Supercond.* **26** 4201305
[26] Bondarenko I *et al* 2013 Technology and tooling to manufacture low-ohm (<2 nΩ) electrical joints of the ITER PF1 coil *IEEE Trans. Appl. Supercond.* **23** 4201605
[27] Pison P F, Langeslag S A E, Santillana I A, Dimitrijevic A, Sgobba S, Ilyin Y, Simon F and Lim B S 2019 The effect of specific manufacturing characteristics on PF ITER full-size joint performance *IEEE Trans. Appl. Supercond.* **29** 4200706
[28] Ilyin Y, Nijhuis A, Abbas W, Bruzzone P, Stepanov B, Muzzi L, Gislon P and Zani L 2016 Effect of cyclic loading and conductor layout on contact resistance of full-size ITER PFCI conductors *IEEE Trans. Appl. Supercond.* **15** 1359–62
[29] Kovalchuk O *et al* 2015 Test of PF1 coil electrical joint *IEEE Trans. Appl. Supercond.* **28** 4205104
[30] Lelekhov S, Tronza V, Bruzzone P, Stepanov B, Bessette D, Devred A and Vostner A 2017 Investigation of RF Nb-Ti PF 1&6 coils conductor performances in the SULTAN test facility *IEEE Trans. Appl. Supercond.* **27** 4200705
[31] Bruzzone P L, Stepanov B, Wesche R, Ilyin Y, Herzog R, Calvi M, Bagnasco M and Cau F 2009 Methods, accuracy and reliability of ITER conductor tests in SULTAN *IEEE Trans. Appl. Supercond.* **19** 1508–11
[32] Breschi M, Cavallucci L, Ribani P L and Gauthier F 2022 Analysis of electrodynamic transients in the ITER PF joints *IEEE Trans. Appl. Supercond.* **32** 4200105
[33] Breschi M, Cavallucci L, Tronza V, Mitchell N, Bruzzone P and Sedlak K 2021 Impact of mechanical and thermal cycles at different operating conditions on the ITER toroidal field coil conductor performance *Supercond. Sci. Technol.* **34** 085021
[34] Ansys Maxwell 3D (available at: www.ansys.com/products/electronics/ansys-maxwell)
[35] Breschi M, Cavallucci L, Ribani P L and Bauer P 2023 Electrodynamic losses of the ITER PF joints during the dynamic plasma scenario *IEEE Trans. Appl. Supercond.* **33** 4200705